Physics-Based Model for Nonuniform Thermionic Electron Emission from Polycrystalline Cathodes

Dongzheng Chen, Ryan Jacobs, John Petillo, Vasilios Vlahos, Kevin L. Jensen, Dane Morgan, and John Booske

Physics-based Model for Nonuniform Thermionic Electron Emission from Polycrystalline Cathodes

Dongzheng Chen,[1] Ryan Jacobs,[1] John Petillo,[2] Vasilios Vlahos,[3] Kevin L. Jensen,[4] Dane Morgan,[1] and John Booske[5]

[1] Department of Materials Science and Engineering,

University of Wisconsin-Madison, 1509 University Ave, Madison, WI 53706, USA

[2] Leidos, 700 Technology Park Dr., Billerica, MA 01821 USA

[3] Viasat Space Systems, 2040 E. Technology Circle, Tempe, AZ 85284 USA

[4] Code 6362, MSTD, Naval Research Laboratory, Washington, DC 20375, USA

[5] Department of Electrical and Computer Engineering, University of Wisconsin-Madison, 1415 Engineering Dr, Madison, WI 53706, USA

Abstract

A new physics-based model is developed that predicts the emitted current from thermionic cathodes that accurately spans from the temperature-limited (TL) to the full-space-charge-limited (FSCL) regions. Experimental observations of thermionic electron emission demonstrate a smooth transition between TL and FSCL regions of the emitted-current-density-versus-temperature ($J - T$) (Miram) curve and the emitted-current-density-versus-voltage ($J - V$) curve. Knowledge of the temperature and shape of the TL-FSCL transition is important in evaluating the thermionic electron emission performance of cathodes, including predicting the lifetime. However, there have been no first-principles physics-based models that predict the smooth TL-FSCL transition region for real thermionic cathodes without applying *a priori* assumptions or empirical phenomenological equations that are physically difficult to justify. Previous work detailing the nonuniform thermionic emission found that the effects of 3-D space charge, patch fields (electrostatic potential

nonuniformity on the cathode surface based on local work function values), and Schottky barrier lowering can lead to a smooth TL-FSCL transition region from a model thermionic cathode surface with a checkerboard spatial distribution of work function values. In this work, we construct a physics-based nonuniform emission model for commercial dispenser cathodes. This emission model is obtained by incorporating the cathode surface grain orientation via electron backscatter diffraction (EBSD) and the facet-orientation-specific work function values from density functional theory (DFT) calculations. The model enables construction of two-dimensional emitted current density maps of the cathode surface and corresponding $J-T$ and $J-V$ curves. The predicted emission curves show excellent agreement with experiment, not only in TL and FSCL regions but, crucially, also in the TL-FSCL transition region. This model provides a method to predict the thermionic emission from the microstructure of a commercial cathode, and improves the understanding of the relationship between thermionic emission and cathode microstructure, which is beneficial to the design of vacuum electronic devices.

I.   Introduction

Thermionic electron emission cathodes based on porous, polycrystalline W combined with mixtures of metal oxides (typically BaO-CaO-Al$_2$O$_3$) marked a significant evolutionary step in the history of thermionic cathodes, as these dispenser cathodes produce high-current-density emission with long lifetime due to their dynamically stable, low-work-function surfaces. [1] There are some widely-used mixture ratios for the metal oxides in the dispenser cathodes. The most common mix is BaO:CaO:Al$_2$O$_3$=5:3:2 (a B-type cathode) which produces emitted current densities of several A/cm^2. There are other variations including the 4:1:1 cathode (S-type), which is resistant to surface poisoning and can usually be operated at a temperature 30°C lower than other types. [2–5] More recent dispenser cathodes include the M-type and scandate cathodes, which have a lower effective work function than the B- and S-type cathodes. [6–8] The B-, S- and M-type cathodes have constituted the majority of commercial thermionic cathodes for the past 50 years and are used as the electron sources in numerous vacuum electronic devices (VEDs) such as communication devices, ion thrusters, thermionic energy converters, and free electron lasers. These applications, taken together, influence multiple facets of our modern life, ranging from defense, satellite

communications, radar, and scientific research, to industrial-scale food production and manufacture of heat-harvesting renewable energy technology. [9,10]

Numerous experimental and computational studies have shown that the microstructure of real W-based cathodes is complex. The tungsten bodies are polycrystalline and porous, and the cathode surfaces are spatially heterogeneous, with the presence of machining marks from the cathode manufacturing process also contributing to the heterogeneity and contributing local field enhancement effects. [4,11–13] One of the results of the complex microstructure is that W-based cathodes are spatially heterogeneous with a distribution of grain sizes and many types of exposed surfaces. These surfaces might have varied crystal facets and metal oxide coatings, each with an associated work function value, leading to highly nonuniform emission. [3,5,6,8,14–17] The nonuniform nature of thermionic electron emission from polycrystalline W has been observed experimentally by using thermionic electron emission microscopy (ThEEM). [16,18–27] In a representative ThEEM image, at a particular temperature, certain grains of the W surface are bright while others remain dark, indicating that some grains are more emissive than others, due to factors such as lower work function, surface topography, etc.

Emitted-current-density-versus-temperature, or $J-T$ (Miram) curves and emitted-current-density-versus-voltage, or $J-V$ ($I-V$) curves are commonly used to evaluate the cathode performance. Both the $J-T$ and $J-V$ curves of a cathode can be divided into three regions: temperature-limited (TL) region, full-space-charge-limited (FSCL) region, and the TL-FSCL transition region. The TL region is in the low-temperature end of an $J-T$ curve or the high-voltage end of an $J-V$ curve. Its behavior can be well described with the Richardson–Laue–Dushman equation [28,29] with Schottky barrier lowering [30]. The FSCL region is in the high-temperature end of a $J-T$ curve or the low-voltage end of a $J-V$ curve. The behavior can be predicted by the Child–Langmuir law [31,32] and Langmuir and Fry's models [32,33], including provision for two-dimensional edge-correction effects [34–40]. Experimental observations on real thermionic cathodes show that the TL-FSCL region is usually smooth, sometimes referred to as the "roll-off". Despite this seemingly simple observed behavior, it has remained an ongoing challenge to develop a physics-based emission model which is able to accurately predict the behavior of both $J-T$ and $J-V$ curves from polycrystalline cathodes over the entire operational domain of temperature and

3

anode-cathode voltage, and especially challenging to capture the smooth transition between the TL and FSCL regions for real cathodes. Thermionic cathodes are typically operated on the FSCL side near the TL-FSCL transition region, so that the changes in cathode temperature over time do not cause large variations to the emitted current and that the emission is stable over the predicted lifetime of the device.

Some empirical descriptions of the smooth TL-FSCL region have been developed, including the empirical Longo–Vaughan equation [41,42], a continuous Gaussian distribution of work function [43], the work function distribution mathematical treatment of emission data [44], and the practical work function distribution (PWFD) [45]. However, all of these models are based on empirical equations or *a priori* assumptions that are difficult to justify, such as the assumption that different work function patches do not interact. Furthermore, these empirical descriptions are not able to reveal the fundamental origin of the smooth behavior of the TL-FSCL transition, thus limiting their usefulness for modeling cathode behavior under different operating conditions.

A number of previous works have studied the interplay of a heterogeneous cathode surface on the resulting thermionic emission and have sought to connect the smooth TL-FSCL transition to the spatial distribution of work function values. The theory of the anomalous Schottky effect [46] studied the contribution of the patch field effect (electrostatic potential nonuniformity on the cathode surface based on local work function values) and the Schottky barrier lowering effect on the smoothness of the TL-FSCL transition in $J - V$ curves. Studies on space charge effects [39,40,47,48] reveal the contribution of 3-D space charge fields on the smooth transition in $J - T$ curves. However, the TL-FSCL transition behaviors predicted from these two separate sets of studies are sharper than experimental observations, indicating that some physical effects are missing. There has been no physics-based emission model which can predict the TL-FSCL transition in agreement with experimental results, although Longo and Vaughan speculated [41,42] that sharper Miram curve knees might be associated with more uniform work function surfaces, or "better" cathodes. Our recent work [49] developed a physics-based model that included the effects of nonuniform thermionic emission, 3-D space charge, patch fields, and Schottky barrier lowering. That work gave a mathematical method to calculate the emitted current from a cathode with a spatially heterogeneous work function distribution in an infinite parallel diode, and was able to

predict a smooth and gradual TL-FSCL transition comparable with experimental observations by using a checkerboard work function distribution. Those findings were encouraging, and indicated our model may be able to predict the emission of a real cathode, including the smooth TL-FSCL transition, by applying a two-dimensional work function map obtained from the same real cathode.

In this work, we construct a two-dimensional work function map by incorporating the grain orientation via electron backscatter diffraction (EBSD) and the facet-orientation-specific work function values from density functional theory (DFT) calculations. We use this work function map in conjunction with the nonuniform emission model developed in our previous work [49] to predict both the J–T (Miram) and J–V (I–V) curves, including the TL-FSCL transition. Overall, we find semi-quantitative agreement of our predicted results with experimental measurements. In this work, a physics-based thermionic emission model incorporating heterogeneous surface effects from a work function distribution on a real commercial thermionic cathode has been used to successfully model the experimental emission over a wide domain of temperature and applied voltage, and illustrates that accurate modeling of the J–T (Miram) and J–V (I–V) characteristics of a real, polycrystalline cathode is practical. Moreover, this work establishes that an experimentally-derived nonuniform work function distribution is able to self-consistently and quantitatively predict the J–T and J–V characteristics of a real, polycrystalline cathode over a very wide range of parameter values, without the need for significant adjustment of any empirical fitting factors.

II. Methods

A. Cathode sample

The cathode analyzed in this work is a commercial S-type cathode made by 3M Technical Ceramics. The cathode was made of 80% density W using standard manufacturing methods and impregnated with an oxide mixture of $BaO:CaO:Al_2O_3$=4:1:1. The cathode was cylinder-shaped with a 2.77 mm diameter and 0.97 mm height, as measured after the emission test. The cathode body is cylindrical in shape, and the surface of the cathode is macroscopically flat.

B. Emission measurement

The experimental results of emitted current were measured in a closely-spaced diode testing vehicle (Fig. 1). The heater and the anode fixtures were manufactured by L3-Harris. The anode-cathode distance in this setup for a 0.97 mm high cathode was designed to be $d = 1.06$ mm. A molybdenum ring was placed around the cathode to shield the emission from the sides. The height of the molybdenum ring was 1.14 mm, which was 0.17 mm higher than the cathode. The inner diameter (ID) 2.90 mm was 0.13 mm larger than the diameter of the cathode. The heater filament was powered by a Keithley 2200-20-5 programmable power supply which was operated under constant current mode.

To make it possible to measure the temperature of the cathode surfaces using a pyrometer during operation, a triode design was used with a hollow cylinder as the current collector, or "catcher". The temperature of the cathode surface was measured with a Catalogue Number 8622 optical pyrometer made by Leeds & Northrup Co., which is a $\lambda = 0.65\,\mu\text{m}$ single-wavelength disappearing filament pyrometer. The electron emission cathode industry often simply uses the pyrometer reading to indicate the cathode temperature, reporting it as the brightness temperature. However, the true temperature of the cathode surface is needed to use our nonuniform emission model [49]. We calibrated the temperature values using Planck's law. The radiation of the cathode received by the disappearing pyrometer at wavelength λ is:

$$tr\epsilon \frac{2hc^2}{\lambda^5} \frac{1}{e^{hc/(\lambda kT)}-1} = \frac{2hc^2}{\lambda^5} \frac{1}{e^{hc/(\lambda kT_b)}-1} \quad (1)$$

where T_b is the pyrometer reading (brightness temperature), T is the calibrated "true" temperature of the cathode surface to be used in the emission model, k is the Boltzmann constant, h is the Planck constant, c is the speed of light. The values of the transmissivity of the viewport $t = 0.93$ and the reflectivity of the mirror $r = 0.76$ in the optical path were as measured. In this study, we used the emissivity value of $\epsilon = 0.52$ recommended for impregnated W cathodes. [2] The uncertainty of the measured temperature values was approximately $\pm 20°\text{C}$.

The cathode was activated before the emission tests, following the instructions recommended by the cathode manufacturer, 3M Technical Ceramics. The activation process includes four steps: (1)

slowly increase the cathode temperature to a brightness temperature of 1000°C, and then hold this temperature for 30 minutes, (2) continue to increase the cathode temperature to a brightness temperature 1175-1200°C and hold for 1 hour, (3) cool the cathode to a brightness temperature 1100-1150°C and hold for 2 hours, and (4) reduce cathode temperature and measure the emitted current while cooling down the cathode. The pressure was kept below 5×10^{-6} torr during the activation process.

During the emission measurements, the grid was biased with a PVX-4110 high voltage pulse generator made by Directed Energy (DEI), which was powered by a DC high voltage power supply made by Glassman High Voltage, Inc. with Model No. PS/ER02R150-115, and controlled by a low voltage pulse generator Model 575 pulse/delay generator made by Berkeley Nucleonics Corp (BNC). The catcher was biased with a DC high voltage power supply made by Glassman High Voltage, Inc. with Model No. PS/EQ005R240-22 and was kept more positively biased than the grid. The voltages of the grid and the catcher were measured with a LeCroy 44Xs oscilloscope. The emitted current was measured with the same oscilloscope via a Model 4100C current monitor made by Pearson Electronics, Inc.
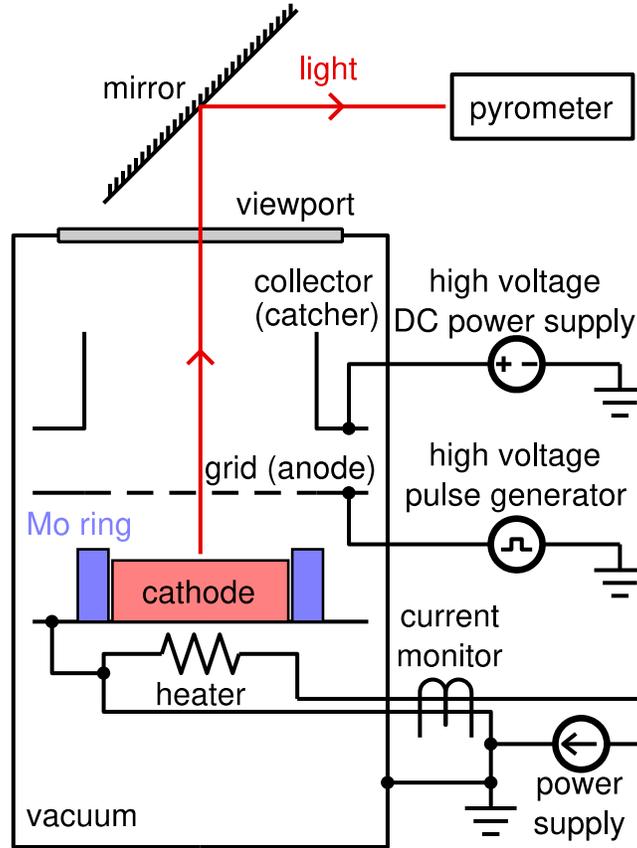
FIG. 1 Sketch of the closely spaced diode testing vehicle used to measure the thermionic emitted current. The rectangle filled with pink is the cathode. The purple rectangles around the cathode represent the molybdenum ring used to shield the side emission.

C. Microstructure characterization

The cathode surface grain orientation was characterized using electron backscatter diffraction (EBSD) in a FEI Helios G4 Plasma FIB/FESEM/EBSD/EDS workstation after the emission test. The surface of commercial dispenser cathodes is usually rough due to the machining process of cutting the cathode pellets on a lathe. The machining typically produces micrometer-scale ridges, and those differences can be seen in variation in emission properties. [50] Confidence index (CI) values in the EBSD results were used to quantify the likelihood of correct grain orientation labeling. [51] CI standardization, one of the built-in clean-up algorithms in OIM Analysis™ by EDAX, a software for EBSD analysis, was used to process the raw EBSD data. Pixels with low CI values after applying the CI standardization clean-up procedure were considered as areas where grain orientations were unable to be correctly labeled by EBSD [52] and the surface facet orientation could not be reliably determined. Visual inspection showed that the majority of pixels

with CI lower than 0.1 were associated with nonemitting areas, such as rough valleys, depressions, grain boundaries, and pores. [53] Thus, areas with $CI < 0.1$ were considered as no-emit areas, and the grain orientation of areas with $CI \geq 0.1$ were considered as recognizable areas. We then used simulations described below to establish a two-dimensional work function map $\phi_{\mathrm{DFT}}(x, y)$ for $CI \geq 0.1$ areas.

D. Density functional theory work function values

Previous density functional theory (DFT) studies have calculated the work functions and surface stabilities of tungsten surfaces with Ba, O, and Ba-O adsorbates of eight different orientations: (001), (011), (111), (210), (211), (221), (310), (311). [5,6,17] Auger analysis indicates that the active state for impregnated cathodes can be reproduced by a near monolayer of the stoichiometric Ba-O on the W surface. [15] Only the DFT work function value for the most stable stoichiometric Ba-O adsorption were used to assign to each orientation (Table I). For a high-index orientation (hkl) other than the calculated eight orientations, the nearest neighbor algorithm was used to predict its work function. [54] It was assumed that a facet with an (hkl) orientation had the same work function as the one among the calculated eight orientations with the smallest misorientation with (hkl) (Fig. 2).
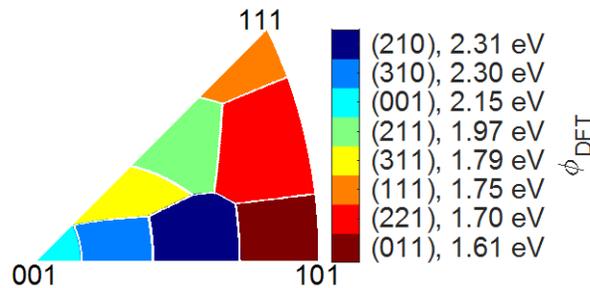
FIG. 2 Inverse polar figure (IPF) showing how a grain orientation is grouped into one of the eight orientation groups using the nearest neighbor algorithm. The colors indicate the work function values assigned to each orientation group, which are the work function values of the W surface with most stable stoichiometric Ba-O adsorption calculated by density functional theory (DFT).

A few studies have estimated the uncertainty of DFT work function values by comparing DFT results with experimental results. De Waele *et al*. [55] compared the experimental work function

values for different surface orientations for a number of metals with the values predicted by the Perdew-Burke-Ernzerhof parametrization of the generalized gradient approximation (PBE-GGA) method. They did a linear fit of DFT values ϕ_{DFT} and experimental values ϕ_{exp}. The result was the equation $\phi_{\mathrm{exp}} = \beta_1 \phi_{\mathrm{DFT}} + \beta_0$, where the values of the fitted coefficients were $\beta_1 = 0.99 \pm 0.02$ and $\beta_0 = 0.30 \pm 0.09$ (eV). Tran *et al.* [56] also compared their DFT results, ϕ_{DFT}, with experimental values, ϕ_{exp}, on single crystals. They made a single-parameter $\phi_{\mathrm{DFT}} = \phi_{\mathrm{exp}} - c$ least square fit, where their result was $c = 0.30$ eV. Both results indicate that DFT work function predictions of metals using GGA-level functionals tend to underestimate the work function values by approximately 0.30 eV, on average, compared with experimental results, and that the error of the estimate is on the scale of tenths of eV even after the linear fit. Due to this known underestimation, we considered the shift between experimental and calculated work function as a fitting parameter in our emission modeling (more details in Section II.E).

E. Emission modeling

It is prohibitively difficult to accurately measure, and thus, to know, the exact anode-cathode distance d at the operating temperatures in our test fixture. Therefore, to better compare the results of the emission model with the experimental results, in this work, we obtained the effective anode-cathode distance d by fitting the FSCL data points with the Child-Langmuir law with the finite temperature correction in an infinite parallel diode [32]:

$$J_{\mathrm{FSCL}} = \frac{4\epsilon_0}{9} \sqrt{\frac{2e}{m}} \frac{(V-V_{\mathrm{m}})^{3/2}}{(d-z_{\mathrm{m}})^2} \frac{9}{8\sqrt{\pi}} \eta^{-\frac{3}{2}} \left(\int_0^\eta \frac{\mathrm{d}\eta}{\sqrt{\mathrm{erfcx}\sqrt{\eta}-1+2\sqrt{\eta/\pi}}} \right)^2 \quad (2)$$

where ϵ_0 is the vacuum permittivity, e is the elementary charge, m is the electron mass, V is the anode-cathode voltage, d is the anode-cathode distance, V_{m} and z_{m} are the voltage and the location from cathode of the voltage minimum, $\eta = e(V - V_{\mathrm{m}})/(kT)$ where k is the Boltzmann constant and T is the temperature, and erfcx is the scaled complementary error function. Instead of using the as-designed value of the anode-cathode distance, we used the fitted value for the emission model, which we believe is a more accurate value for high temperatures during emission measurements. Based on our experience and that of others, the use of a cathode-diameter-to-gap-ratio of approximately 3, and the use of the molybdenum edge emission suppression ring are

sufficient to enable using the infinite-area form of Eq. 2 to estimate the anode-cathode gap under high temperature.

In the theory of the Child-Langmuir law with the finite temperature correction on a uniform cathode, [32] the voltage minimum satisfies the Richardson-Laue-Dushman equation: $J = AT^2 \exp[-eV_m/(kT)]$, while the voltage minimum position $z_m = 0$ at the TL-FSCL transition. When fitting d using Eq. 2, we made the same assumptions: $z_m = 0$ and $J = AT^2 \exp[-eV_m/(kT)]$, where J is the experimentally measured emitted current density. Here, $A = 4\pi m e k^2/h^3 = 120.173$ A $/\text{cm}^{-2}$ K^{-2} is the Richardson constant where h is Planck's constant.

It is not practical to do EBSD on the whole surface of a cathode, so we characterized the grain orientation on a representative area of the cathode surface (more details in Section III.D), and used periodic boundary conditions on the edges of the work function map, considering that the nonuniform emission model [49] was designed for spatially periodic work function maps. Considering the error in the DFT work function values, we added a constant shift $\Delta\phi$ on the DFT work function values, $\phi_{DFT}(x, y)$, to get a shifted work function map, $\phi(x, y) = \phi_{DFT}(x, y) + \Delta\phi$, for the $CI \geq 0.1$ areas.

The roughness of the thermionic cathode used in this study was mainly due to machining and the grain structures. The range of the field enhancement factor values expected from the roughness features of typical thermionic cathodes is usually small, with an estimated upper bounds of 5. [12,50,57,58] Even in the case that the applied electric field is 500 V/mm, the difference in the Schottky barrier lowering between a surface with a field enhancement factor of $\beta = 5$ and a perfectly flat surface $\beta = 1$ is only 0.033 eV, which will add a negligible enhancement to the thermionic emission, compared with the uncertainty of the DFT work function values. Therefore, for simplicity in our model, we assumed the cathode surface was perfectly flat and neglected field enhancement effects.

The grain orientations of areas with $CI \geq 0.1$ were considered as recognizable, and a work function map $\phi(x, y) = \phi_{DFT}(x, y) + \Delta\phi$ was assigned to these areas. By choosing to assign a uniform reference value of zero to the cathode's Fermi energy, the boundary condition of Poisson's

equation for each $CI \geq 0.1$ area was its vacuum level $V(x, y, z = 0) = -\phi(x, y)/e$. [49] Meanwhile, as the majority of $CI < 0.1$ pixels were associated with nonemitting areas, such as rough valleys, depressions, grain boundaries, and pores, [53] we obtained the boundary conditions, $V(x, y, z = 0)$, for the cathode surface's $CI < 0.1$ areas by solving the 2-D Laplace's equation $\nabla^2 V(x, y) = 0$. For the 2-D boundary value at each edge of a $CI < 0.1$ area, we used the V value of the adjacent $CI \geq 0.1$ area. In this way, we obtained the boundary condition of the whole cathode surface, for both $CI \geq 0.1$ areas and $CI < 0.1$ areas, which was the input of the nonuniform emission model [49]. There was only one fitting parameter, $\Delta\phi$, in this model.

In the model, the potential energy for an electron present in the space within the diode is obtained by solving Poisson's equation, where the charge density is a nonlinear function of the potential energy in the space. The effect of Schottky barrier lowering is included when calculating the potential energy. The patch field effect is naturally included in the non-equipotential boundary condition at the cathode surface $V(x, y, z = 0)$, and 3-D Poisson's equation includes the 3-D space charge effect. Therefore, such a nonuniform emission model includes the effects of 3-D space charge, patch fields, and Schottky barrier lowering, but neglects the effects of the lateral motion of electrons and the quantum effects (e.g., electron tunneling). More information on the physics and specific calculation methodology of our nonuniform emission model can be found in Ref. [49].

III. Results and Discussion

A. Spatial distribution of work function

We used EBSD to characterize the spatial distribution of grain orientation for a particular cathode after the emission testing was concluded on that cathode sample. We chose this ordering to ensure that our EBSD measurements captured any microstructural evolution that may have occurred during the high temperature activation and emission testing processes. Fig. 3a shows the two-dimensional maps of grain orientation of a representative portion of a cathode surface (more details in Section III.D). The percentage of each orientation group in the map is listed in Table I.

We measured the emitted current from a commercial S-type cathode made by 3M Technical Ceramics (Section II.A) for various anode-cathode voltages and temperatures (Fig. 4). The anode-cathode distance d was obtained by fitting the FSCL data points using Eq. 2. In this work, we used the 24 data points above 1340 K in Fig. 4a as the FSCL data points to obtain the anode-cathode distance d, and the result was $d = 1.132$ mm. As expected, this is very close to the designed value of 1.06 mm. We ascribe the discrepancy between the fitted distance and the designed value to several reasonable factors that include a likely small difference between the designed distance and the actual fabricated distance (at room temperature) as well as the effects of electron optics and thermal expansion. The constant work function shift was obtained by fitting all the data points in Fig. 4a with the nonuniform emission model, and the result was $\Delta\phi = 0.176$ eV, which indicates that DFT underestimated the work function values compared with the thermionic emission test results. This result is consistent with previous studies on the error of DFT predicted work function values [55,56] in both the sign and magnitude of the error (underestimation by DFT of approximately 0.3 eV). Fig. 3b is the predicted work function map, obtained by applying shifted DFT work function values to the grain orientation map (Fig. 3a).

(a)

111

001   101

(b)

No emit
(210), 2.486 eV
(310), 2.476 eV
(001), 2.326 eV
(211), 2.146 eV
(311), 1.966 eV
(111), 1.926 eV
(221), 1.876 eV
(011), 1.786 eV

$\phi_{DFT} + \Delta\phi$
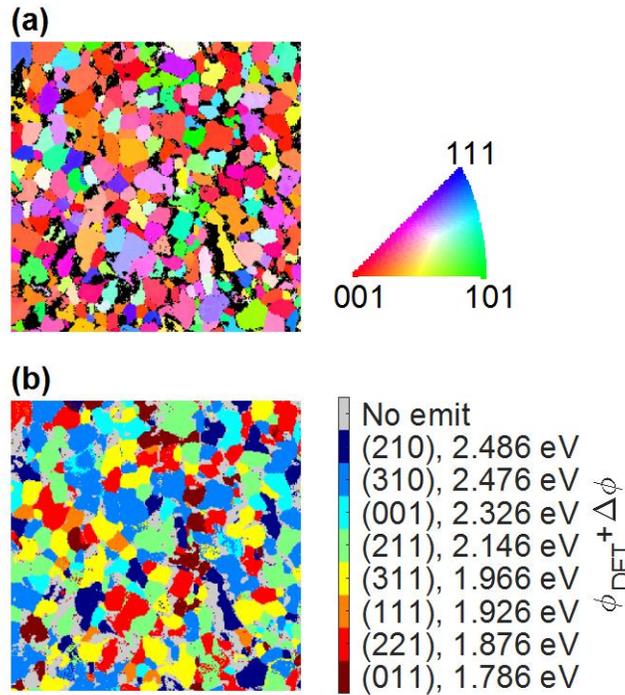
FIG. 3 (a) Electron backscatter diffraction (EBSD) inverse polar figure (IPF) of a commercial S-type cathode after clean-up. The areas where it is considered that grain orientations are

unrecognized by EBSD are plotted in black. (b) Work function map by assigning the density functional theory (DFT) work function value [5] with a shift of $\Delta\phi = 0.176$ eV to the grain orientation map (a) after grouping the orientations into one of the eight orientation groups.

TABLE I. List of the eight orientations with work function values predicted using density functional theory (DFT). ϕ_{DFT} is the DFT work function value for the most stable stoichiometric Ba-O adsorption for each orientation. $\phi_{\text{DFT}} + \Delta\phi$ is the shifted work function value where the shift is $\Delta\phi = 0.176$ eV. The "Percentage" column shows the percentage of each orientation group in Fig. 3.

Orientation	ϕ_{DFT} (eV)	$\phi_{\text{DFT}} + \Delta\phi$ (eV)	Percentage
(001)	2.15	2.326	6.3%
(011)	1.61	1.786	5.5%
(111)	1.75	1.926	2.3%
(210)	2.31	2.486	8.9%
(211)	1.97	2.146	14.0%
(221)	1.70	1.876	12.7%
(310)	2.30	2.476	19.3%
(311)	1.79	1.966	13.8%
Unrecognized	-	-	17.1%

B. Emitted current density

Fig. 4 shows the experimental emission data from the S-type cathode (× and + symbols), the emitted current density predicted by applying the nonuniform emission model [49] (solid curves) to the work function map (Fig. 3b), and the results predicted from a uniform cathode with a single work function value (dotted curves).

The physics of nonuniform thermionic emission was not well-studied before our work. It is conventional to use a single work function value (a so-called "effective" work function) to describe the emission performance of a heterogeneous, nonuniform thermionic cathode [59]. Scott and Eng's theoretical model [60,61] unifies the inclusion of the Schottky effect and space charge effect, and therefore is able to predict the TL, FSCL, and the TL-FSCL transition regions for a uniform cathode with a single work function value in an infinite parallel diode. To investigate the consequence of applying their model, we assumed that our S-type cathode sample can be described with a single work function value ϕ, and obtained its value by fitting all the data points in Fig. 4a with Scott and Eng's theoretical model. The result was $\phi = 2.021$ eV, which falls within the range of the local work function values listed in Table I. Fig. 4a shows that the approach of using a single

effective work function can fit the TL and FSCL asymptotes in the $J - T$ curves. However, this uniform cathode model is not able to accurately reproduce the smooth TL-FSCL transition from experimental observations. Fig. 4b further reveals that such a single work function value approach cannot predict the Schottky line (high voltage asymptote in the $J - V$ curves) observed in polycrystalline thermionic cathodes. Although the uniform cathode model with a single work function value is a simplified and well-studied model, it is not sufficient to predict some of the complex physical behavior present in the $J - T$ and $J - V$ curves from polycrystalline cathodes.

Such limitations of the uniform cathode model motivate our present work for developing a nonuniform emission model. For the same S-type cathode sample, Fig. 4 shows that our nonuniform emission model is in semi-quantitative agreement with experimental measurements, including predicted TL-FSCL transition regions that are as smooth as the experimental observations for both the $J - T$ and $J - V$ curves and predicted Schottky lines that are in good agreement with the high V asymptotes in the experimentally measured $J - V$ curves. The gap between model and experimental results is significantly reduced by introducing the nonuniformity and relevant physical effects into the model.
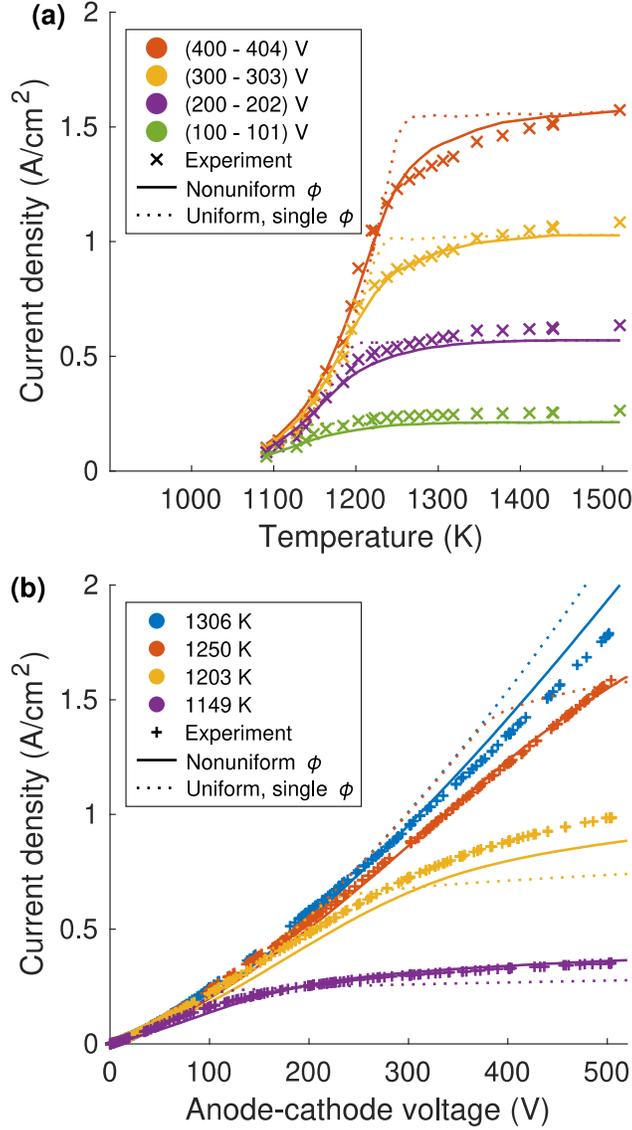
FIG. 4 Experimental data ($\times$ and $+$ symbols) of an S-type cathode compared with the emitted current density predicted with nonuniform emission model (solid curves) and the results predicted with a uniform cathode with a single fitted work function value (dotted curves). (a) $J - T$ curves for different anode-cathode voltages V. Different colors denote different measured V values: red for data between 400 V and 404 V, $300\,\mathrm{V} \leq V \leq 303\,\mathrm{V}$ for yellow, $200\,\mathrm{V} \leq V \leq 202\,\mathrm{V}$ for purple, and $100\,\mathrm{V} \leq V \leq 101\,\mathrm{V}$ for green. (b) $J - V$ curves, where different colors denote different temperatures.

There are only two fitting parameters in our model: the anode-cathode distance $d = 1.132$ mm and the constant shift on DFT work function values $\Delta\phi = 0.176$ eV. The main effect of a different d is to scale up and down the FSCL current, while the effect of a different $\Delta\phi$ is to scale up and down the TL current or shift the TL region to a lower or higher temperature in $J - T$ curves. Using

fitted values for these two parameters helps to get a better fit for the TL and FSCL regions, enabling a better comparison on the TL-FSCL transition regions between predicted curves and experimental results. The exact values of both of these fitted parameters have negligible effects on the shape of the TL-FSCL transition region. (More details in Supplemental Material [62])

The smooth TL-FSCL transition in the predicted curves arises as a natural consequence of the nonuniform emission from the polycrystalline cathode with a nonuniform spatial distribution of work function. Previous studies [39,40,47,48] show that the 3-D space charge effect plays a significant role in making the transition region smooth for a nonuniform cathode. However, when using a work function map for a real cathode derived from DFT and EBSD, a model only considering the 3-D space charge effect predicts a TL-FSCL transition in a Miram curve sharper than experimental results. [47] The nonuniform emission model used in this work [49] includes all of the effects of 3-D space charge, patch fields, and Schottky barrier lowering. This result shows that including all of these effects is required to predict the smooth TL-FSCL transition region in the $J - T$ and $J - V$ curves, not only for the checkerboard model cathode illustrated in [49], but also in a work function map of a real cathode.

The Richardson constant A is an important factor in the Richardson-Laue-Dushman equation. Its theoretical value is $A = 4\pi m k_\mathrm{B}^2 e/h^3 = 120.173 \, \mathrm{A \, cm^{-2} K^{-2}}$. In multiple previous studies, the Richardson constant was experimentally obtained by fitting both the Richardson constant and the effective work function in the Richardson-Laue-Dushman equation to the experimental emission data under the assumption that the cathode is uniform and has a single work function value. [59] It has been observed that, using this method, the experimental values of the Richardson constant differ from the theoretical value, sometimes by many orders of magnitude. [43,59] However, the Richardson constant does not need to be fit in our model, and is assumed to be fixed to its theoretical value. The agreement between our experimental and predicted $J - T$ and $J - V$ curves indicates that the alteration of the Richardson constant is not needed here. Thus, a key strength of our present model is that knowledge of the fractions of different surface terminations present, their arrangement in 2D space on the surface, and their work functions are all that is required for the nonuniform emission model to provide a physically complete picture of the emission.

C. Two-dimensional emission map

Fig. 5 shows how the calculated emitted current density maps change as temperature increases and the emission changes from the temperature-limited (TL) region (Fig. 5a) to the transition region (Fig. 5b and 5c), and finally to the full-space-charge-limited (FSCL) region (Fig. 5d). To better illustrate the effects of the patch fields and space charge, we plotted schematic figures of equipotential curves and electric flux lines in the space in front of a low work function patch surrounded by high work function patches in TL, transition, and FSCL regions (Fig. 6).

In the TL region (Fig. 5a), the space charge effect is negligible, and therefore the low work function patches emit more than the high work function patches. The result that the emitted current density varies across different grains due to the difference in their work function values (ϕ) is consistent with experimental thermionic electron emission microscopy (ThEEM) images obtained in the TL region. [16,18–27]

As the schematic figures show, in the TL region (Fig. 6a), the space charge effect is negligible, so the electrostatic potential in this case is close to the solution of the 3-D Laplace's equation $\nabla^2 V(x,y,z) = 0$. The nonuniform boundary condition at the cathode surface $V(x,y,z=0) = -\phi(x,y)/e$ introduces additional electric fields between different work function patches besides the applied electric field between the anode and the cathode. Therefore, the equipotential contours and electric flux lines are bent in the space close to the patch boundaries. Such additional electric fields between different patches are referred to as the patch fields. The patch fields lead to a voltage minimum (potential depression, also called as the virtual cathode) occurring a short distance above the edges of the strongly-emitting low-ϕ patch. This causes the local emitted current density $J(x,y)$ at the edge of low-ϕ patches to be smaller than the center of the patches (Fig. 5a). [46,63,64] In the transition region (Fig. 5b) this patch field effect continues to depress low work function patches' edge currents relative to their center currents, even though a potential depression begins to form above the patch center due to the space charge effect (Fig. 6b). Note that the reduced edge emission of low work function patches due to patch fields contrasts with enhanced edge emission on a cathode surface with nonuniform emission but without patch field effects. In the latter case, the edges of high-emitting patches emit more than the center of the patches due to the lower space charge in front of their neighboring low-emitting patches. [36,37,40]

In the transition and FSCL regions (Fig. 6b, 6c, and 6d), the more strongly-emitting, low-ϕ patches have more significant space charge effects than the less-emitting, high-ϕ patches. As observed in Fig. 6b and 6c, the strongly-emitting, low-ϕ patches develop voltage minima above their surfaces at these transition region temperatures. This space charge effect limits the emission from the low-ϕ patches while the emission from the high-ϕ patches continues to increase without such limitation. This 3D space charge effect causes the emission to become increasingly more spatially uniform as the temperature increases from the transition region to the FSCL region (Fig. 5b, 5c, and 5d).

In our nonuniform emission model, even though electrons are restricted along the cathode-anode direction with no lateral momentum, our model is able to predict the trend of the change in the emission nonuniformity as temperature changes. Such a trend has also been observed in experiments [65,66] and is consistent with some previous computational studies [39,40,47,48].
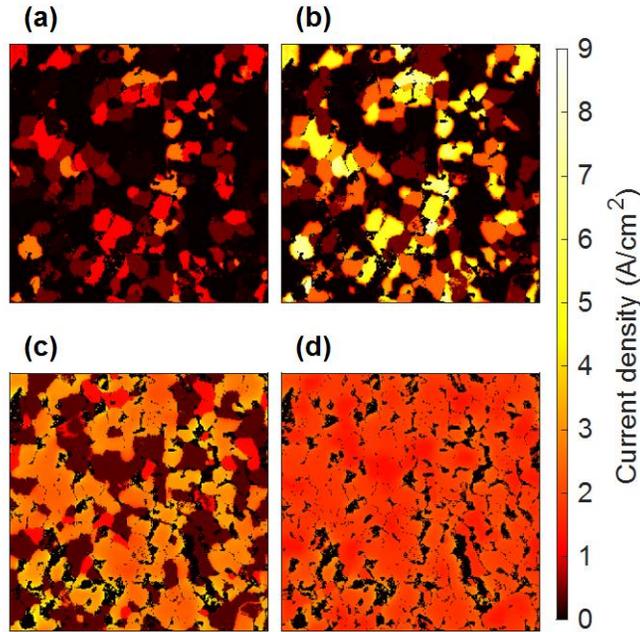
FIG. 5 Emitted current density maps $J(x, y)$ predicted using nonuniform emission model for a cathode with work function map as Fig. 3b at anode-cathode voltage $V = 400$ V and distance $d = 1.132$ mm, at different temperatures: (a) TL region: temperature $T = 1149$ K, average emitted current density $J = 0.340$ A/cm^2, (b) transition region: 1250 K, $J = 1.234$ A/cm^2, (c)

transition region but with an average emitted current density close to the full-space-charge-limited (FSCL) value: 1411 K, $J = 1.525$ A/cm^2, (d) FSCL region: 1521 K, $J = 1.552$ A/cm^2.
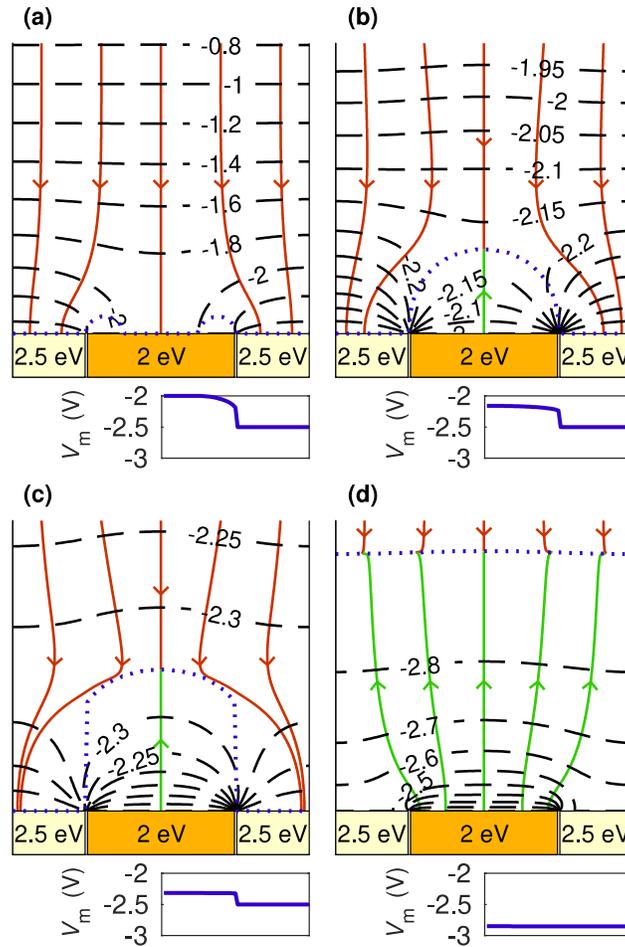
FIG. 6 Schematic figures illustrating the effects of patch fields and 3-D space charge in different regions: (a) temperature-limited (TL) region, (b) transition region, (c) transition region with an average emitted current density close to full-space-charge-limited (FSCL) value, and (d) FSCL region. The anode (not shown in the figures) is far away above the top of each subfigure, and the cathode is on the bottom of each subfigure, with a low work function patch (2 eV) surrounded by high work function patches (2.5 eV). Dashed black curves are the equipotential contours of the electrostatic potential (unit: V). The red and green solid curves are the electric flux lines. The red ones are for the electric flux lines starting from the anode while the green ones for those starting from the cathode. The dotted violet curves indicate the position of voltage minimum $z_m(x, y)$ (position of the virtual cathode). The plots beneath each subfigure (solid violet curves) show the value of the voltage minimum in front of different location of the cathode surface $V_m(x, y)$. The value of $V_m(x, y)$ on the left half (not plotted) is symmetric to the right half. The local emitted current density is $J(x, y) = AT^2 \exp[-eV_m/(kT)]$.

20

D. Sensitivity analysis and sources of error

It is computationally expensive to simulate large areas (for example, 0.1 mm^2 or larger) with the nonuniform emission model and time-consuming to characterize the grain orientation of a large area where there are a large number of grains. The computational cost is significantly increased in beam optics simulations where millions of time steps are typically used. [67] To determine the representativeness of the statistics of the surface facets and ascertain the relationship between the uncertainty of the predicted emitted current and the size of the work function map, we characterized a total of 9 EBSD maps with size of $128 \text{ μm} \times 128 \text{ μm}$ on different regions of the S-type cathode, for a total examined area of 0.15 mm^2, and calculated the resulting emitted current density as a function of the examined area of the cathode surface.

To evaluate the effect of the uncertainty in the work function values to the predicted emitted current density, we calculated the emitted current density from a work function map by applying $\phi(hkl) = \phi_{\text{DFT}}(hkl) + \Delta\phi(hkl)$ to the grain orientation map in Fig. 3a, where the (hkl) is one of the eight grain orientations assigned with DFT work function values, and the work function shift for the eight grain orientations $\Delta\phi(hkl)$ are assumed to be independent and identically distributed (i.i.d.) following the normal distribution $\Delta\phi(hkl) \sim N(0.176 \text{ eV}, \sigma_{\text{DFT}}^2)$, where the standard deviation σ_{DFT} represents a phenomenological error in our DFT measurements. We have generated 2500 random work function maps for each σ_{DFT} value and calculated the variability of their emitted current densities.

Fig. 7 shows the variability of the values of the emitted current density for different submap sizes (Fig. 7a) and different uncertainties of work function values (Fig. 7b) at a condition for the TL-FSCL transition region. Fig. 7a shows how the prediction of the emitted current density becomes more precise as the size of the submap increases, which indicates that model users may determine the submap size to use according to their desired precision in the prediction. Fig. 7b estimates the uncertainty in the predicted emitted current density as a function of the uncertainty in the work function values. Previous studies [55,56] estimated that the error of the DFT predicted work function values is on the scale of tenths of eV. Our results show that even in the extreme case that the DFT work function values have an uncertainty of 0.4 eV, the median (the red line in the box in Fig. 7b) is 1.29 A/cm^2, close to 1.23 A/cm^2, which was the result for the baseline case ($\phi =$

$\phi_{\text{DFT}} + 0.176$ eV, Fig. 4 and 5b). In the $\sigma_{\text{DFT}} = 0.4$ eV results, the first quartile (the lower edge of the box) is $Q_1 = 1.11$ A/cm^2 while the third quartile (the upper edge) is $Q_3 = 1.41$ A/cm^2, and the interquartile range is IQR $= Q_3 - Q_1 = 0.29$ A/cm^2. Such a dispersion is smaller than using a 32 μm × 32 μm submap, which has IQR $= 0.37$ A/cm^2, indicating a robustly predicted average current density even for the higher end of DFT work function uncertainty values.
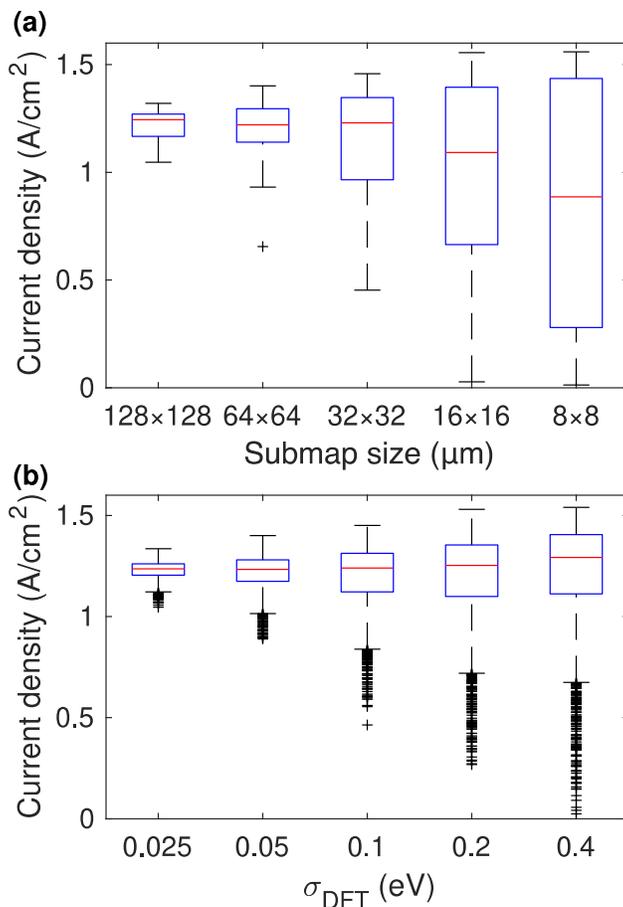
FIG. 7 Boxplots showing the variability of the emitted current density predicted (a) from the submaps of different characterized area sizes at temperature $T = 1250$ K, anode-cathode voltage $V = 400$ V and distance $d = 1.132$ mm, (b) from a work function map by applying $\phi(hkl) = \phi_{\text{DFT}}(hkl) + \Delta\phi(hkl)$ to the grain orientation map in Fig. 3a, where the shift values are independent and identically distributed (i.i.d.) following the normal distribution $\Delta\phi(hkl) \sim N(0.176$ eV, $\sigma_{\text{DFT}}^2)$. In a boxplot, the red line in the box indicates the median value. The lower edge of the box is the first quartile (Q_1 or 25th percentile). The upper edge is the third quartile (Q_3 or 75th percentile). The interquartile range (IQR) is defined as IQR $= Q_3 - Q_1$. Data points larger than $Q_3 + 1.5$IQR or smaller than $Q_1 - 1.5$IQR are considered as outliers and plotted individually using the $+$ symbols. The whiskers extend to the most extreme data points not considered to be outliers.

Other possible causes of the error in the predicted emitted current density include the measurement error in temperature values, the dependence of the work function value on temperature due to different stable arrangements of Ba-O surface species at different temperatures, and the dependence of the anode-cathode distance on temperature due to thermal expansion. The assumptions in the nonuniform emission model [49] may also contribute to the error in the predicted emission, which include the assumption of a perfectly flat cathode surface in an infinite parallel diode, neglecting the lateral motion of the electrons, and neglecting the quantum effects. While it is beyond the scope of the present work to perform an in-depth investigation of the role of each of these sources of error, we find it very encouraging that the results in Fig. 4 illustrate that our model shows near quantitative agreement with experiment over a wide range of temperatures and anode-cathode voltages. This strong agreement with experiment suggests that while many sources of uncertainty in our model exist, they likely play a minor role in the resulting emission compared with the microstructural features of the cathode, including the fractions of each surface present, their size and spatial distribution, and the relative work functions of grains comprising the cathode surface.

IV.   Conclusions and Outlook

Our nonuniform emission model can predict two-dimensional maps of emitted current density and therefore the average emitted current densities at different temperatures and anode-cathode voltages based on a two-dimensional work function map derived by DFT calculations and microstructure characterization. Importantly, the predicted $J - T$ and $J - V$ curves are in semi-quantitative agreement with experimental results, including the nature of the TL-FSCL transition, which shows the same shape as experiments. There are only two fitting parameters in our model: the anode-voltage distance and a constant shift on the DFT work function values. The effect of these two fitting parameters on the shape of the TL-FSCL transition is negligible. Our model uses a physics-based modeling method coupled with experimental characterization to reproduce experimental emission data, and illustrates that it is not necessary to use an empirical equation such as the Longo-Vaughan equation or to assume a continuous work function distribution. A key result of this work is that a smooth TL-FSCL transition region is a natural consequence of the

physics of the nonuniform emission from a spatial distribution work function map when the effects of 3-D space charge, patch fields, and Schottky barrier lowering are included.

The present findings provide both a robust physics-based approach to predict the emitted current from any polycrystalline cathode for which the surface grain orientations and work functions are known, and a means to understand how the cathode microstructure and the underlying work functions couple to the expected emission behavior. The present "forward" model starts from cathode work function distributions and predicts $J - T$ and $J - V$ curves. In the future, it may be possible to create an "inverse" model where one starts from experimentally measured $J - T$ and/or $J - V$ curves and predicts an effective cathode work function arrangement and associated microstructure consistent with the measured emission. Such an approach may be an effective method to better understand the coupling of cathode microstructure with the measured emission of new cathodes. Such a method would provide a powerful tool for understanding the expected emission behavior of new cathodes, as conducting an emission test on a new cathode is less time-consuming than a full suite of microstructure and work function studies, e.g., using EBSD characterization and DFT calculations. The results in this work can also be used as input for higher-level simulation codes like MICHELLE [67] to improve the modeling of cathodes in electron gun fixtures, better informing device design and enabling deeper insight into the physical factors governing heterogeneous emission from thermionic cathodes.

Raw data of the figures are available in Supplemental Material [62]. Codes for the nonuniform emission model are available on GitHub (https://github.com/chen-dongzheng/nonuniform-emission).

Acknowledgements

References

[1] D. M. Kirkwood, S. J. Gross, T. J. Balk, M. J. Beck, J. Booske, D. Busbaher, R. Jacobs, M. E. Kordesch, B. Mitsdarffer, D. Morgan, W. D. Palmer, B. Vancil, and J. E. Yater, *Frontiers in Thermionic Cathode Research*, IEEE Trans. Electron Devices **65**, 2061 (2018).

[2] J. . Cronin, *Modern Dispenser Cathodes*, IEE Proc. I Solid State Electron Devices **128**, 19 (1981).

[3] V. Vlahos, Y.-L. Lee, J. H. Booske, D. Morgan, L. Turek, M. Kirshner, R. Kowalczyk, and C. Wilsen, *Ab Initio Investigation of the Surface Properties of Dispenser B-Type and Scandate Thermionic Emission Cathodes*, Appl. Phys. Lett. **94**, 184102 (2009).

[4] A. Gilmour, *Klystrons, TWTs, Magnetrons, Crossed-Field Amplifiers, and Gyrotrons* (Artech House, 2011).

[5] R. Jacobs, D. Morgan, and J. Booske, *Work Function and Surface Stability of Tungsten-Based Thermionic Electron Emission Cathodes*, APL Mater. **5**, 116105 (2017).

[6] Q. Zhou, X. Liu, T. Maxwell, B. Vancil, T. J. Balk, and M. J. Beck, *BaxScyOz on W (001), (110), and (112) in Scandate Cathodes: Connecting to Experiment via MO and Equilibrium Crystal Shape*, Appl. Surf. Sci. **458**, 827 (2018).

[7] X. Liu, Q. Zhou, T. L. Maxwell, B. K. Vancil, M. J. Beck, and T. J. Balk, *Scandate Cathode Surface Characterization: Emission Testing, Elemental Analysis and Morphological Evaluation*, Mater. Charact. **148**, 188 (2019).

[8] J. Wang, Y. Yang, Y. Wang, W. Liu, M. Zhou, and T. Zuo, *A Review on Scandia Doped Tungsten Matrix Scandate Cathode*, Tungsten **1**, 91 (2019).

[9] R. J. Barker, N. C. Luhmann, J. H. Booske, and G. S. Nusinovich, *Modern Microwave and Millimeter-Wave Power Electronics* (2005).

[10] J. H. Booske, *Plasma Physics and Related Challenges of Millimeter-Wave-to-Terahertz and High Power Microwave Generation*, Phys. Plasmas **15**, 055502 (2008).

[11] D. Jones, D. McNeely, and L. W. Swanson, *Surface and Emission Characterization of the*

Impregnated Dispenser Cathode, Appl. Surf. Sci. **2**, 232 (1979).

[12] K. L. Jensen, D. W. Feldman, M. Virgo, and P. G. O'Shea, *Measurement and Analysis of Thermal Photoemission from a Dispenser Cathode*, Phys. Rev. Spec. Top. - Accel. Beams **6**, 083501 (2003).

[13] Y. Wan, Y. Li, Q. Wang, K. Zhang, and Y. Wu, *The Relationship of Surface Roughness and Work Function of Pure Silver by Numerical Modeling*, Int. J. Electrochem. Sci. **7**, 5204 (2012).

[14] R. Forman, *Surface Studies of Barium and Barium Oxide on Tungsten and Its Application to Understanding the Mechanism of Operation of an Impregnated Tungsten Cathode*, J. Appl. Phys. **47**, 5272 (1976).

[15] G. A. Haas, A. Shih, and C. R. K. Marrian, *Interatomic Auger Analysis of the Oxidation of Thin Ba Films*, Appl. Surf. Sci. **16**, 139 (1983).

[16] D. Norman, R. A. Tuck, H. B. Skinner, P. J. Wadsworth, T. M. Gardiner, I. W. Owen, C. H. Richardson, and G. Thornton, *Surface Structure of Thermionic-Emission Cathodes*, Phys. Rev. Lett. **58**, 519 (1987).

[17] V. Vlahos, J. H. Booske, and D. Morgan, *Ab Initio Investigation of Barium-Scandium-Oxygen Coatings on Tungsten for Electron Emitting Cathodes*, Phys. Rev. B **81**, 054207 (2010).

[18] G. A. Haas and R. E. Thomas, *Work- Function Distribution Studies of Pressed Matrix Cathodes*, J. Appl. Phys. **38**, 3969 (1967).

[19] M. V. Mroz, T. Savina, M. E. Kordesch, J. T. Sadowski, and S. A. Tenney, *Solid-Solid Dewetting of Scandium Thin Films on the W(100) Surface Observed Using Emission Microscopy*, J. Vac. Sci. Technol. B **37**, 012903 (2019).

[20] R. A. Tuck, *Surface Studies of Thermionic Emitters by Methods Unique to Them*, Appl. Surf. Sci. **2**, 128 (1979).

[21] C. Wan, J. M. Vaughn, J. T. Sadowski, and M. E. Kordesch, *Scandium Oxide Coated Polycrystalline Tungsten Studied Using Emission Microscopy and Photoelectron Spectroscopy*, Ultramicroscopy **119**, 106 (2012).

[22] J. M. Vaughn, K. D. Jamison, and M. E. Kordesch, *In Situ Emission Microscopy of Scandium/Scandium-Oxide and Barium/Barium-Oxide Thin Films on Tungsten*, IEEE Trans. Electron Devices **56**, 794 (2009).

[23] J. M. Vaughn, K. D. Jamison, and M. E. Kordesch, *17.3: Work Function Reduction by Multilayer Oxides :Thermionic Electron Emission Microscopy of Scandium Oxide and Barium Oxide on Tungsten*, in *2010 IEEE International Vacuum Electronics Conference (IVEC)* (IEEE, 2010), pp. 421–422.

[24] M. E. Kordesch and C. Wan, *Barium De-Wetting and Thermionic Emission from Ba on W*, in *2013 26th International Vacuum Nanoelectronics Conference (IVNC)* (IEEE, 2013), pp. 1–2.

[25] C. Wan and M. E. Kordesch, *Tungstate Formation in a Model Scandate Thermionic Cathode*, J. Vac. Sci. Technol. B, Nanotechnol. Microelectron. Mater. Process. Meas. Phenom. **31**, 011210 (2013).

[26] F. Ren, S.-Y. Yin, Z.-P. Lu, Y. Li, Y. Wang, S.-J. Zhang, F. Yang, and D. Wei, *Applications of Deep Ultraviolet Laser Photo-and Thermal-Emission Electron Microscope in Thermal Dispenser Cathode Research*, Acta Phys. Sin. **66**, 187901 (2017).

[27] M. Mroz, S. Tenney, T. Savina, and M. E. Kordesch, *Thermionic Emission Microscopy of Scandium Thin Film Dewetting on W(100)*, AIP Adv. **8**, 065114 (2018).

[28] O. W. Richardson, *"The Emission of Electricity from Hot Bodies.,"* J. Röntgen Soc. **18**, 150 (1922).

[29] S. Dushman, *Thermionic Emission*, Rev. Mod. Phys. **2**, 381 (1930).

[30] W. Schottky, *Über Kalte Und Warme Elektronenentladungen*, Zeitschrift Für Phys. **14**, 63 (1923).

[31] C. D. Child, *Discharge From Hot CaO*, Phys. Rev. (Series I) **32**, 492 (1911).

[32] I. Langmuir, *The Effect of Space Charge and Initial Velocities on the Potential Distribution and Thermionic Current between Parallel Plane Electrodes*, Phys. Rev. **21**, 419 (1923).

[33] T. C. Fry, *The Thermonic Current between Parallel Plane Electrodes; Velocities of Emission Distributed According to Maxwell's Law*, Phys. Rev. **17**, 441 (1921).

[34] J. W. Luginsland, Y. Y. Lau, and R. M. Gilgenbach, *Two-Dimensional Child-Langmuir Law*, Phys. Rev. Lett. **77**, 4668 (1996).

[35] Y. Y. Lau, *Simple Theory for the Two-Dimensional Child-Langmuir Law*, Phys. Rev. Lett. **87**, 278301 (2001).

[36] R. J. Umstattd and J. W. Luginsland, *Two-Dimensional Space-Charge-Limited Emission:*

Beam-Edge Characteristics and Applications, Phys. Rev. Lett. **87**, 145002 (2001).

[37] J. W. Luginsland, Y. Y. Lau, R. J. Umstattd, and J. J. Watrous, *Beyond the Child–Langmuir Law: A Review of Recent Results on Multidimensional Space-Charge-Limited Flow*, Phys. Plasmas **9**, 2371 (2002).

[38] Y.-M. QUAN and Y.-G. DING, *Generalization of the Two-Dimensional Child–Langmuir Law for Non-Zero Injection Velocities in a Planar Diode*, J. Plasma Phys. **75**, 85 (2009).

[39] A. Sitek, K. Torfason, A. Manolescu, and Á. Valfells, *Space-Charge Effects in the Field-Assisted Thermionic Emission from Nonuniform Cathodes*, Phys. Rev. Appl. **15**, 014040 (2021).

[40] A. Sitek, K. Torfason, A. Manolescu, and Á. Valfells, *Edge Effect on the Current-Temperature Characteristic of Finite-Area Thermionic Cathodes*, Phys. Rev. Appl. **16**, 034043 (2021).

[41] R. T. Longo, *A Study of Thermionic Emitters in the Regime of Practical Operation*, in *1980 International Electron Devices Meeting* (IRE, 1980), pp. 467–470.

[42] R. Vaughan, *A Synthesis of the Longo and Eng Cathode Emission Models*, IEEE Trans. Electron Devices **33**, 1925 (1986).

[43] A. S. Gilmour, *Principles of Traveling Wave Tubes* (Artech House, 1994).

[44] J. C. Tonnerre, D. Brion, P. Palluel, and A. M. Shroff, *Evaluation of the Work Function Distribution of Impregnated Cathodes*, Appl. Surf. Sci. **16**, 238 (1983).

[45] M. Cattelino and G. Miram, *Predicting Cathode Life Expectancy and Emission Quality from PWFD Measurements*, Appl. Surf. Sci. **111**, 90 (1997).

[46] L. K. Hansen, *Anomalous Schottky Effect*, J. Appl. Phys. **37**, 4498 (1966).

[47] D. Chernin, Y. Y. Lau, J. J. Petillo, S. Ovtchinnikov, D. Chen, A. Jassem, R. Jacobs, D. Morgan, and J. H. Booske, *Effect of Nonuniform Emission on Miram Curves*, IEEE Trans. Plasma Sci. **48**, 146 (2020).

[48] A. Jassem, D. Chernin, J. J. Petillo, Y. Y. Lau, A. Jensen, and S. Ovtchinnikov, *Analysis of Anode Current From a Thermionic Cathode With a 2-D Work Function Distribution*, IEEE Trans. Plasma Sci. 1 (2021).

[49] D. Chen, R. Jacobs, D. Morgan, and J. Booske, *Impact of Nonuniform Thermionic Emission on the Transition Behavior Between Temperature-and Space-Charge-Limited Emission*, IEEE Trans. Electron Devices **68**, 3576 (2021).

[50] K. L. Jensen, Y. Y. Lau, and N. Jordan, *Emission Nonuniformity Due to Profilimetry Variation in Thermionic Cathodes*, Appl. Phys. Lett. **88**, 164105 (2006).

[51] D. P. Field, *Recent Advances in the Application of Orientation Imaging*, Ultramicroscopy **67**, 1 (1997).

[52] M. M. Nowell and S. I. Wright, *Orientation Effects on Indexing of Electron Backscatter Diffraction Patterns*, Ultramicroscopy **103**, 41 (2005).

[53] S. I. Wright and M. M. Nowell, *EBSD Image Quality Mapping*, Microsc. Microanal. **12**, 72 (2006).

[54] D. Chen, R. Jacobs, V. Vlahos, D. Morvan, and J. Booske, *Statistical Model of Non-Uniform Emission/Rom Polycrystalline Tungsten Cathodes*, in *2019 International Vacuum Electronics Conference (IVEC)* (IEEE, 2019), pp. 1–2.

[55] S. De Waele, K. Lejaeghere, M. Sluydts, and S. Cottenier, *Error Estimates for Density-Functional Theory Predictions of Surface Energy and Work Function*, Phys. Rev. B **94**, 235418 (2016).

[56] R. Tran, X.-G. Li, J. H. Montoya, D. Winston, K. A. Persson, and S. P. Ong, *Anisotropic Work Function of Elemental Crystals*, Surf. Sci. **687**, 48 (2019).

[57] R. Miller, Y. Y. Lau, and J. H. Booske, *Electric Field Distribution on Knife-Edge Field Emitters*, Appl. Phys. Lett. **91**, 1 (2007).

[58] R. Miller, Y. Y. Lau, and J. H. Booske, *Schottky's Conjecture on Multiplication of Field Enhancement Factors*, J. Appl. Phys. **106**, (2009).

[59] V. S. Fomenko, *Handbook of Thermionic Properties* (Springer US, Boston, MA, 1966).

[60] J. B. Scott, *Extension of Langmuir Space‐ charge Theory into the Accelerating Field Range*, J. Appl. Phys. **52**, 4406 (1981).

[61] G. Eng, *A New Correction to Schottky Barrier Lowering in Cathodes*, J. Appl. Phys. **58**, 4365 (1985).

[62] See Supplemental Material at [URL will be inserted by publisher] for more detailed discussion in the fitted values of work function and anode-cathode distance and the raw data of the figures.

[63] J. A. Becker, *Thermionic Electron Emission and Adsorption Part I. Thermionic Emission*, Rev. Mod. Phys. **7**, 95 (1935).

[64] C. Herring and M. H. Nichols, *Thermionic Emission*, Rev. Mod. Phys. **21**, 185 (1949).

[65] J. Li, H. Wang, Y. Gao, H. Yuan, K. Pan, K. Zhang, Q. Chen, T. Yan, F. Liao, J. Wang, Y. Wang, and W. Liu, *Recent Developments in Scandia-Doped Dispenser Cathodes*, in *2006 IEEE International Vacuum Electronics Conference Held Jointly with 2006 IEEE International Vacuum Electron Sources* (IEEE, 2006), pp. 51–52.

[66] J. Li, H. Wang, Z. Yu, Y. Gao, Q. Chen, and K. Zhang, *Emission Mechanism of High Current Density Thermionic Cathodes*, in *2007 IEEE International Vacuum Electronics Conference*, Vol. 2440 (IEEE, 2007), pp. 1–2.

[67] J. Petillo, K. Eppley, D. Panagos, P. Blanchard, E. Nelson, N. Dionne, J. DeFord, B. Held, L. Chernyakova, W. Krueger, S. Humphries, T. McClure, A. Mondelli, J. Burdette, M. Cattelino, R. True, K. T. Nguyen, and B. Levush, *The Michelle Three-Dimensional Electron Gun and Collector Modeling Tool: Theory and Design*, IEEE Trans. Plasma Sci. **30**, 1238 (2002).